www.acsnano.org

Maximized Frequency Doubling through the Inverse Design of Nonlinear Metamaterials

Lakshmi Raju, Kyu-Tae Lee, Zhaocheng Liu, Dayu Zhu, Muliang Zhu, Ekaterina Poutrina, Augustine Urbas, and Wenshan Cai*



Downloaded via GEORGIA INST OF TECHNOLOGY on March 31, 2022 at 13:44:56 (UTC). See https://pubs.acs.org/sharingguidelines for options on how to legitimately share published articles.

Cite This: ACS Nano 2022, 16, 3926-3933



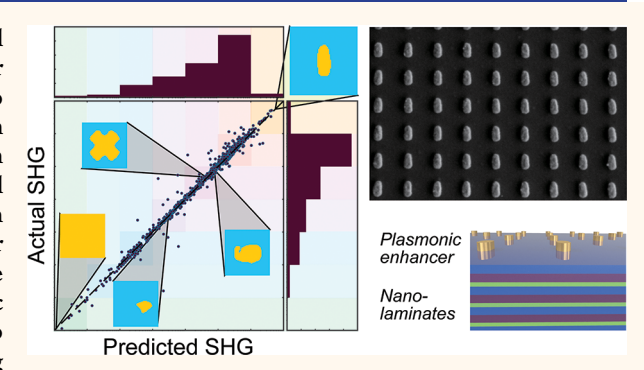
ACCESS I

Metrics & More

Article Recommendations

Supporting Information

ABSTRACT: The conventional process for developing an optimal design for nonlinear optical responses is based on a trial-and-error approach that is largely inefficient and does not necessarily lead to an ideal result. Deep learning can automate this process and widen the realm of nonlinear geometries and devices. This research illustrates a deep learning framework used to create an optimal plasmonic design for a nonlinear metamaterial. The algorithm produces a plasmonic pattern that can maximize the second-order nonlinear effect of a nonlinear metamaterial. A nanolaminate metamaterial is used as a nonlinear material, and plasmonic patterns are fabricated on the prepared nanolaminate to demonstrate the validity and efficacy of the deep learning



algorithm. The optimal pattern produced yielded second-harmonic generation from the nanolaminate with normal incident fundamental light. The deep learning architecture applied in this research can be expanded to other optical responses and light-matter interaction processes.

KEYWORDS: nanophotonics, metamaterial, nonlinear optics, deep learning, plasmonics

he essence of deep learning is to learn from sizable data sets using algorithms loosely arising from models of biological nervous systems. Deep learning has evolved quite rapidly in the past few years, outgrowing the designation as a subset of machine learning. The basic application of a deep learning model is that, once it is trained on a labeled set of data, it can perform classification of data using artificial neural networks (ANN) with multiple layers of artificial neurons—hence the term "deep" learning. The power of the ANN's increasing complexity allows for the achievement of accuracy that can equal and sometimes even exceed human performance.

In general, inverse design in photonics is a method used to identify a set of parameters to define a photonic structure or device given the desired optical responses. This contrasts with traditional design processes of a back and forth, trial and error method starting with candidate patterns from empirical guesses, using parametric sweeps to slightly adjust parameters, and at times never reaching the desired goal due to limitations such as computing power, or geometric candidates. Since the use of ANN's for inverse design can lead to fast, accurate, and sometimes counterintuitive results that cannot be achieved by traditional methods, it has been at the forefront of many research problems as large as wind turbine design and even for smaller applications such as plasmonics. 11–15

Plasmonics is a field that studies and utilizes the optical properties of metal—dielectric interfaces on nanometer-scale structures. Plasmonic structures can serve as unit cells for metamaterials to find previously unseen phenomena or to prove existing theories. Periodic unit cells, such as a plasmonic structure, lead to a metamaterial whose properties are drawn from the periodic structure, as well as the individual cells. ^{16–18}

When designing plasmonic metamaterials and metasurfaces for various design objectives, the linear optical regime, such as spectral control, dispersion engineering, and beam steering, has been well-researched. Whereas, in the nonlinear regime, there is much to be explored. Optical nonlinear processes include frequency mixing, such as second-harmonic generation (SHG), sum-frequency generation, and optical rectification, as well as the Pockels effect and optical Kerr effect. Nonlinear optics is essential for the generation of additional spectral components and active control of light.

Received: October 20, 2021 Accepted: February 10, 2022 Published: February 14, 2022





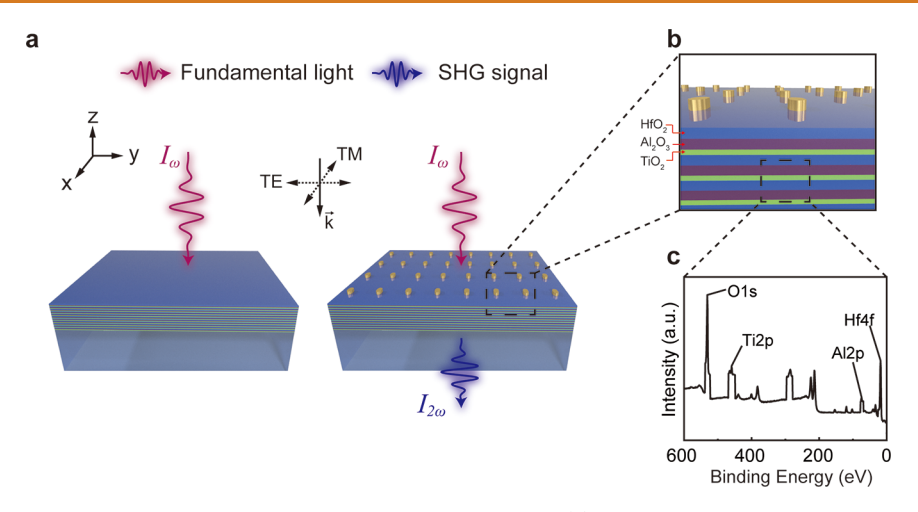


Figure 1. Illustration of metamaterial device, as well as the material composition. (a) Schematic illustration of the ABC nanolaminate devices and definition of the TE and TM polarization of the incident fundamental light. Without plasmonic structures to generate an electric field with a z-component, the ABC nanolaminate will not emit a substantial second-harmonic response in the z-direction. (b) Nanolaminate comprised of three periodic layers, TiO₂, Al₂O₃, and HfO₂. The plasmonic structure is patterned above the nanolaminate. (c) XPS survey spectra of the fabricated ABC nanolaminate consisting of TiO₂, Al₂O₃, and HfO₂.

While bulk thin-film nonlinear materials like LiNbO₃ are commercially available, an easy to fabricate and thinner film is possible using an ABC nanolaminate. ^{22–25} An ABC nanolaminate is a nonlinear metamaterial created using a repetition of thin films of three different layers, an A, B, and C layer, repeated as ABCABC. When using materials that have inversion symmetry, such as silicon, under the electron dipole approximation, there are no even order nonlinear effects, such as second-order effects, meaning there is no nonlinear susceptibility of the second type. At each of the layer interfaces, such as at A-B, or B-C, centrosymmetry is broken in the axis normal to the layers. Once the centrosymmetry is broken, there can be second-order nonlinear effects, or a nonlinear susceptibility in the bulk material along the perpendicular direction. 22-25 To utilize the break in centrosymmetry, the incident light is at an angle in order to possess a nonzero field component along the axial direction, inducing a second-order nonlinear susceptibility. With a TiO₂-Al₂O₃-HfO₂ ABC nanolaminate, following the material and geometric parameters from the successful demonstration by Alloatti et al., the manmade nonlinear oxide composite requires a simple deposition technique, such as atomic layer deposition (ALD), and can have an easily controllable thickness on the order of tens of nanometers, whereas thinfilm bulk materials require complicated growth methods to get a crystalline structure, and typically the thickness is on the order of hundreds of nanometers.²² The ABC nanolaminate is also a better choice, as it is compatible with silicon, which potentially enables numerous integrated optics applications on CMOS compatible platforms. Silicon is very important for integrated optics but is limited for second-order nonlinear optics due to its centrosymmetry.

There has been recent related research that discusses applications of inverse design and nonlinear optics using materials which have nonzero nonlinear optical susceptibilities.^{26–31} The purpose of this research is to use inverse design to identify an optimal plasmonic structure in order to induce the second-harmonic generation and maximize the efficiency of the SHG of an ABC nanolaminate, where the second-order response is zero at normal incidence. The deep learning algorithm finds the relationship between the parameters, the

field profile, the $\chi^{(2)}$, and the SHG response to provide an optimal pattern for the metamaterial. The optimized plasmonic structure is designed with strong field confinement near the ABC nanolaminate and augmented symmetry engineering near the ABC nanolaminate, which will induce the second-harmonic generation in the ABC nanolaminate due to the electric field distribution in the few tens of nanometers range. Using tailored algorithms to solve the challenging inverse design problem, previously unsolvable with conventional methods, of arbitrary topology with almost infinite degrees of freedom, the inverse design will allow the optimization of the metal pattern with user-defined constraints. This can be easily extended to output best possible patterns for a number of scenarios given additional data relating to the other parameters, for example a different nonlinear material, or periodicity.

RESULTS AND DISCUSSION

The goal of this research is to use a deep learning framework to find a metamaterial structure with an arbitrary plasmonic structure atop a nonlinear ABC composite material, that induces a maximal SHG response from the ABC composite. The pattern that will be fabricated as the plasmonic structure is based on a 64 × 64 canvas, meaning the inverse design problem essentially has over 24096 degrees of freedom. Employing deep learning allows the solution of this problem, which cannot be solved through the use of traditional parameter sweeping methods or conventional geometries, for true optimization. The general parameters for the metamaterial shown in Figure 1a are periodicity, p = 360 nm, thickness of the ABC composite, $t_{ABC} = 75$ nm, thickness of the gold plasmonic structure, $t_{\rm Au}=45$ nm, and normal incident wavelength, $\lambda_{\omega}=850$ nm. For the ABC composite, the individual layers also had specified thicknesses as seen in Figure 1b, the thickness of the Al_2O_3 layers, $t_{Al2O_3} = 0.9$ nm, the thickness of the HfO_2 layers, $t_{HfO2} = 0.9$ nm, and the thickness of the TiO_2 layers, $t_{TiO_2} = 0.3$ nm. However, for the simulation portion of this research, the ABC nanolaminate was treated as a homogenized material with nonlinear susceptibilities. The nonlinear polarization of the layered structures with geometric features along the z-axis is calculated using this equation

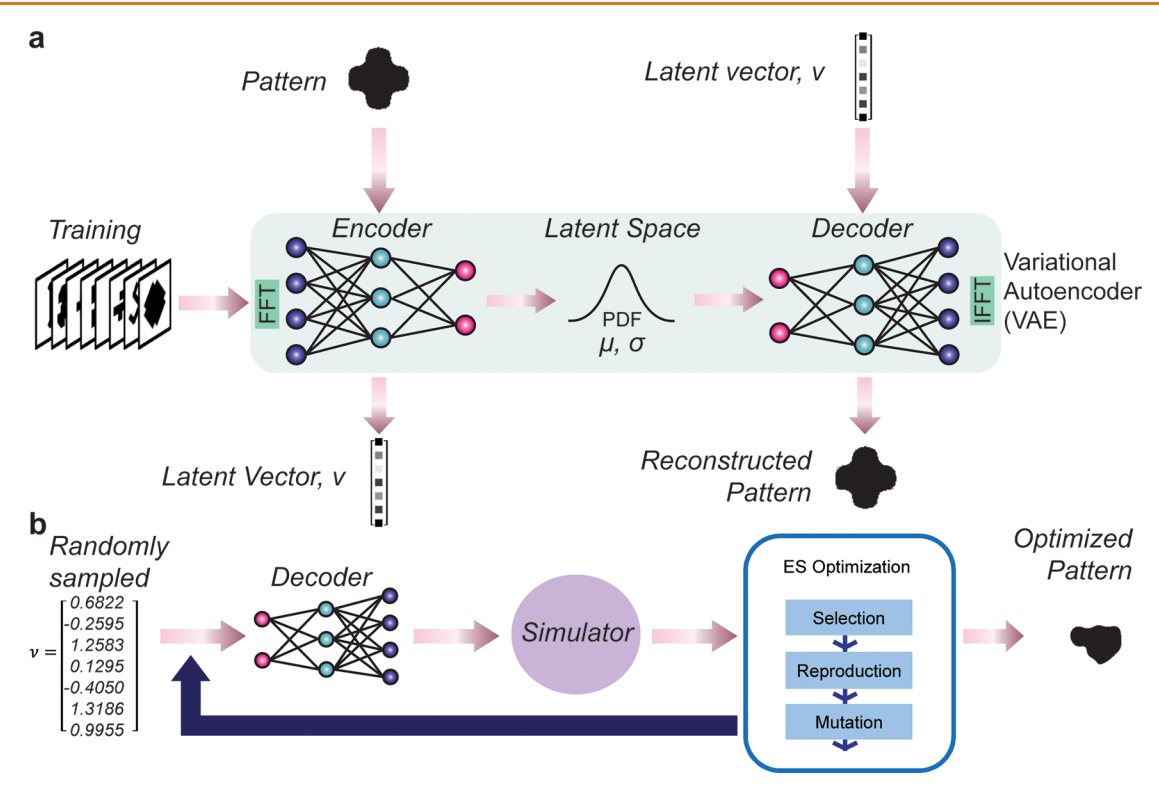


Figure 2. General deep learning framework. (a) Overall flow of the generator, an algorithm used to represent the patterns in the training data using a probability density function (PDF). The generator is based on a variational autoencoder (VAE), and the PDF is used by the encoder and decoder to represent a pattern as a latent vector, v, through "encoding", and then transform v into a reconstructed pattern through "decoding". (b) By randomly sampling v, we can use the decoder from the generator to create patterns. These patterns are passed through the simulator, and a predicted SHG response is output. In order to optimize a pattern to a specific SHG response, an optimizer based on an evolution strategy (ES) is utilized. Passing through a system of selection, reproduction, and mutation, the optimizer circles back to try different v's searching for better patterns until the closest fit is found. The final output is the best pattern for the desired parameters and SHG response.

$$\begin{pmatrix}
P_{x}(2\omega) \\
P_{y}(2\omega) \\
P_{z}(2\omega)
\end{pmatrix} = \epsilon_{0} \begin{pmatrix}
0 & 0 & 0 & \chi_{xxz} & 0 \\
0 & 0 & 0 & \chi_{xxz} & 0 & 0 \\
\chi_{zxx} & \chi_{zxx} & \chi_{zzz} & 0 & 0 & 0
\end{pmatrix}$$

$$\begin{pmatrix}
E_{x}(\omega)^{2} \\
E_{y}(\omega)^{2} \\
E_{z}(\omega)^{2} \\
2E_{y}(\omega)E_{z}(\omega) \\
2E_{x}(\omega)E_{y}(\omega)
\end{pmatrix}$$
(1)

where

$$P_{x}(2\omega) = 2\epsilon_{0}\chi_{xxz}E_{x}(\omega)E_{z}(\omega)$$

$$P_{y}(2\omega) = 2\epsilon_{0}\chi_{xxz}E_{y}(\omega)E_{z}(\omega)$$

$$P_{z}(2\omega) = \epsilon_{0}\chi_{zxx}(E_{x}(\omega)^{2} + E_{y}(\omega)^{2}) + \epsilon_{0}\chi_{zzz}E_{z}(\omega)^{2}$$
(2)

and the $\chi^{(2)}$ susceptibilities used are χ_{zzz} = 0.667 pm/V, χ_{xxz} = 0.254 pm/V, and χ_{zxx} = 0.225 pm/V.

Deep Learning Framework. In order to optimize an arbitrary pattern to create a plasmonic structure that can induce a maximal SHG response from an ABC nanolaminate, a

deep learning framework is used, as parameter-sweeping and standard geometries cannot yield the most enhanced SHG response. The framework can be broken into three parts, the generator, the simulator, and the optimizer. The generator is used to create 2D patterns that translate into the plasmonic structure on top of the nonlinear material. Once patterns can be generated, the simulator uses the generator to find the related SHG response. To target a desired nonlinear response, the optimizer is used to find the best pattern for the response requested. The generator algorithm is based on a variational autoencoder (VAE), as shown in Figure 2a.³⁵

First, 10 000 arbitrary created patterns (64 \times 64 pixel images) form a training set for the generator. The canvas that the patterns are confined to is 64 × 64 pixels, which is important as it creates essentially unlimited possibilities for patterns rather than drawing traditional geometries. This can be further explained as a single pixel turning "on" or "off" leading to a different pattern, so patterns are drawn in a completely different method than a user might create shapes such as nanorods, bow-ties, elliptical patterns, etc. The patterns are then passed through an encoder, which is a neural network. The purpose of the encoder is to "encode" the data into a latent space, or probability density function, with a standard deviation, σ , and mean, μ , which represents all the possible patterns. Then, a randomly sampled latent vector, v, can be fed to a decoder, which is another neural network, based on the same latent space, and be "decoded" into a pattern. If a pattern is encoded, the output is a latent vector, and if that same v is

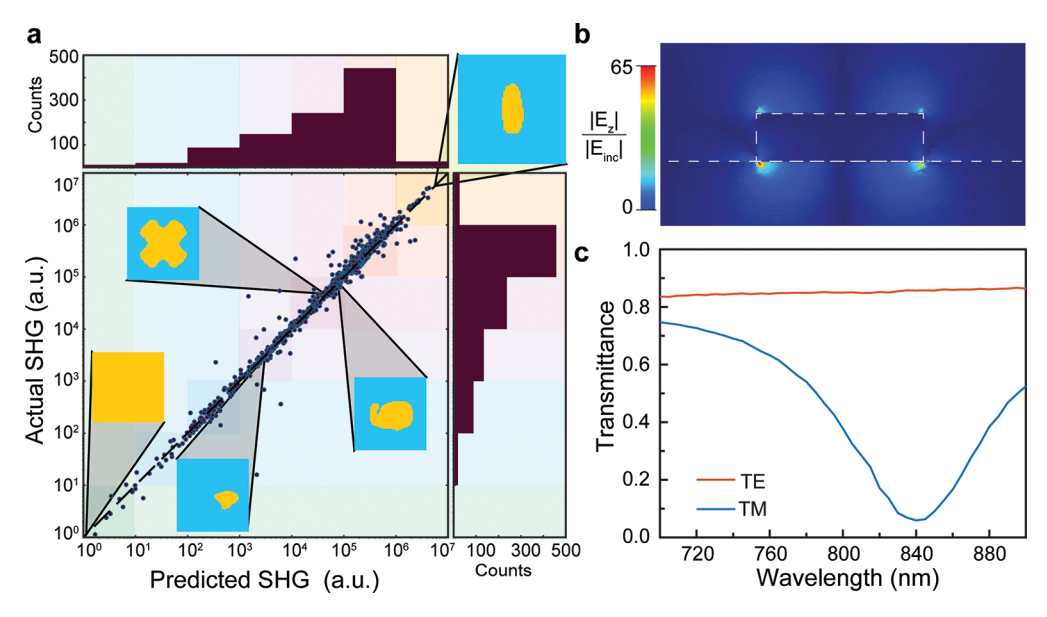


Figure 3. Linear and nonlinear simulations based on deep learning algorithm. (a) The scatter plot is a comparison of the predicted SHG enhancement values from the deep learning simulator and the actual SHG enhancement values from a full-wave simulation for the same set of patterns. The dotted line represents x = y, and the strong correlation between the line and scattered points shows that the simulator is very accurate for a wide range of SHG enhancement values. The error of the simulator for predicting SHG responses is +31.8% and -14.2%. As SHG responses are very sensitive to minor variations in parameters in the full-wave simulation, this error is considered accurate for this research. The histogram above the graph represents the spread of the predicted SHG enhancement values for the patterns from the simulator, and the histogram to the right represents the distribution of actual SHG enhancement values for the same patterns from a full-wave simulation. The SHG enhancement was calculated based on an unpatterned surface. The inset patterns in the graph are examples of patterns from the highlighted points in the scatter plot. The pattern in the top right is the pattern used for further simulation and fabrication in the paper. (b) Cross-sectional view, along the central x-direction or the length of the pattern, of the normalized z-component of the electric field with incident TM polarized light at a wavelength of 840 nm. The strong field enhancement due to the TM polarized light indicates that the SHG response induced in the ABC nanolaminate will be much higher when exposed to TM polarized light as compared to TE polarized light. (c) Calculated transmission spectra for TE and TM polarized light on the plasmonic ABC nanolaminate device.

input into the decoder, the output will be a reconstruction of the input image. The generator allows for the creation of patterns that were not in the original data set, which can lead to a pattern with a response better than if inverse design was not utilized.

The simulator is based on the architecture of ResNet18 and is used to predict the SHG response for the input image. To train the simulator, 10 000 patterns are created from the generator. These patterns are then run through a full-wave simulation to find the actual SHG responses. The fundamental light electric field components are used to calculate the electric field components of the nonlinear response using the induced polarization of the ABC composite. Data collected from the full-wave simulation is used to train the simulator. Once trained, the generator is used to produce patterns for the simulator to predict respective SHG responses.

We adapted an evolution strategy as our optimizer in the framework, as shown in Figure 2b. 32,36 Through a process of selection, reproduction, and mutation, while evaluating a fitness score for the pattern, patterns that maximize the SHG response are created. The accuracy of the simulator can be seen in Figure 3a, where 1000 patterns randomly produced from the generator, to act as a representative sample of the simulator output, are run through both the full-wave simulation for the accurate SHG value, and the simulator, for the predicted value. The dotted line highlights the 1–1 correlation between the two. The histograms show that the spread of SHG values follows an expected curve for both the full-wave simulation data and simulator data. The whole image illustrates the reliability and accuracy of the simulator

algorithm. The optimizer is used to identify the pattern with the highest SHG response for the given parameters, and the resulting pattern is shown in the top right corner of Figure 3a.

The linear response, field enhancement and transmittance, of the identified optimal plasmonic structure was calculated using a full-wave simulation, as shown in Figure 3b,c, respectively. Referring to eq 2, the linear electric field response is integral to the induced second-order response in the ABC nanolaminate. In essence, the simulator is finding a correlation between the pattern of the plasmonic structure and the related electric field components and then predicting the corresponding second harmonic generation. The plasmonic structure induces an electric field with a z-component, and the resonance in the linear response shows that a wavelength of 840 nm with TM-polarized light will lead to the most effective field enhancement. To confirm that the specific features in the optimal pattern from the deep learning algorithm give rise to the optimal SHG response, and not the general shape, a fullwave simulation comparison is applied. A regular ellipse unit cell of similar dimensions to the unique ovoid unit cell shows an SHG response that is \sim 6% of the optimal pattern. This further establishes the deep learning simulation as a tool for the inverse design of plasmonic structures, and the usefulness of the algorithm to find unique geometries. The ellipse pattern used for the confirmation can be found in the Supporting Information. Utilizing the optimal field enhancement leads to a maximal SHG response from the ABC nanolaminate.

Experimental Results. For the experiments of this research, two devices are fabricated—a device with the ABC nanolaminate and the gold pattern as well as an alumina

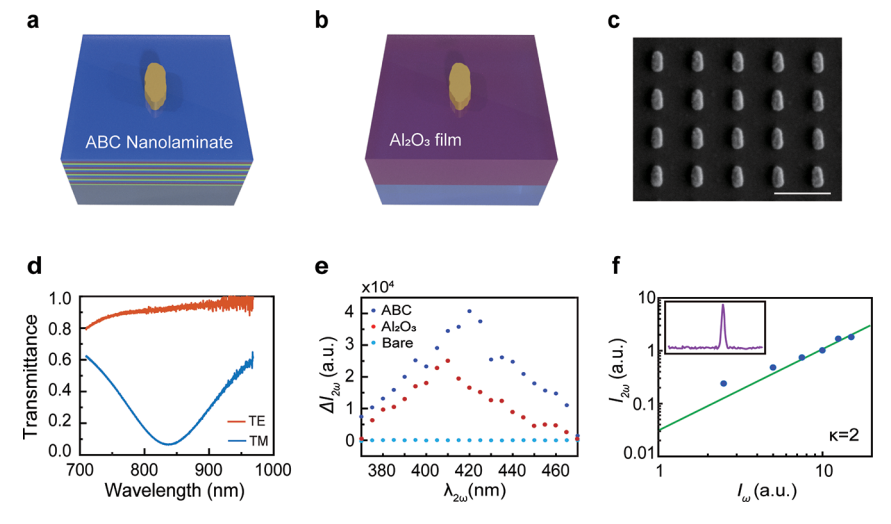


Figure 4. Enhancement of the SHG from the ABC nanolaminate with the deep-learning designed plasmonic structure as well as linear and nonlinear measurements for the ABC nanolaminate device. (a, b) Visualization of a unit cell of ABC nanolaminate device, and the control alumina device with an Al₂O₃ film, both with the same deep-learning optimized gold structure on the surface. (c) SEM image of the fabricated plasmonic structure on the ABC nanolaminate. The scale bar at the bottom represents 500 nm. (d) Experimental linear transmission spectra for TE and TM polarized light. The linear response for the ABC nanolaminate device is similar to the calculated linear response in Figure 3. The resonance wavelength of 840 nm will be used as the fundamental wavelength for subsequent nonlinear measurements. (e) Experimental SHG responses of the respective devices. The blue and red dots are from patterned ABC and alumina devices. The cyan dots represent the response from bare, unpatterned ABC nanolaminate. (f) Power dependence of the ABC patterned nanolaminate. The green line in the double logarithmic plot represents a slope of 2, confirming the second-order nature of the response. The inset shows the SHG spectrum for an incident wavelength of 850 nm measured from 370 to 470 nm, to show the nature of the second-harmonic response.

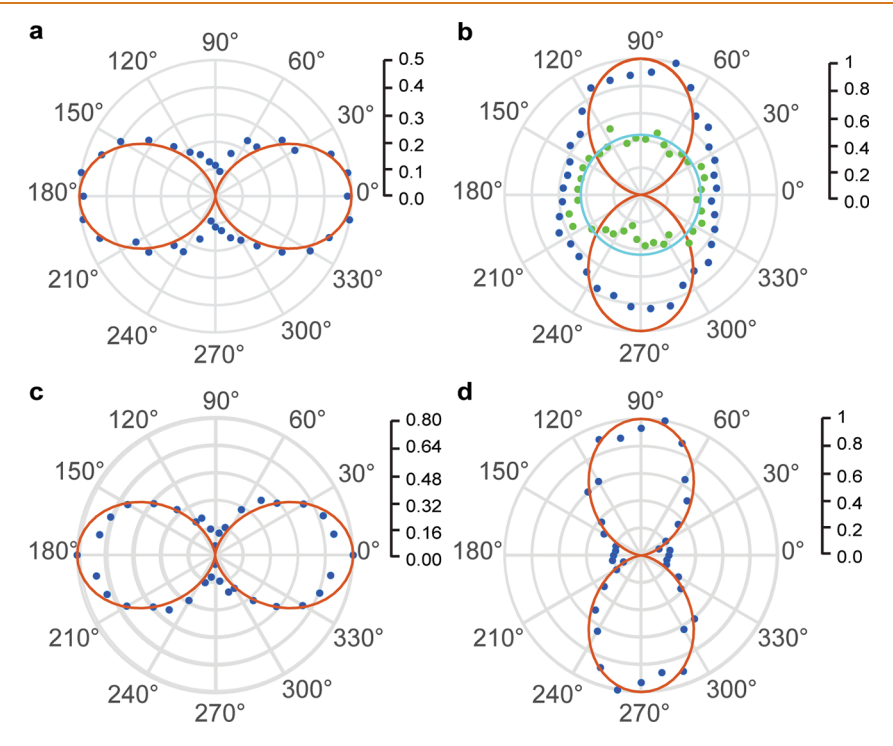


Figure 5. Induced second-harmonic response from ABC nanolaminate and SHG output polarization results for the devices. (a, b) For the patterned ABC device, the SHG output polarization in plotted in polar plots for TE and TM polarized incident fundamental light, respectively. The blue dots are the measured SHG response, and the red curve is the calculated SHG response. In b, the green dots represent the SHG response induced from the ABC nanolaminate. The cyan circle best fits the SHG due to the ABC nanolaminate. (c, d) SHG output polarization plots for the patterned control device for TE and TM polarized incident fundamental light, respectively. The measured second-harmonic signal values are the blue dots, and the calculated second-harmonic response is shown as the red curve. We expected the TE polarized incident light to lead to similar responses in the patterned ABC device and the control device, and that is seen in a and c. The loss of linear polarization observed in a and b indicate that the second-harmonic response does not stem solely from the plasmonic structure, and that is further confirmed by the degeneration of the peanut shape in b.

control device with an Al₂O₃ layer of the same thickness, replacing the ABC nanolaminate layer, below the same gold pattern, as shown in Figure 4a,b. The purpose of the alumina control device is to measure the nonlinear response due to the gold nanoparticle, to eventually differentiate the SHG response due to the ABC nanolaminate and the SHG response from the gold structure. To ensure that the ABC nanolaminate was fabricated correctly, an XPS analysis was done, and the results are displayed in Figure 1c which demonstrates that all three oxides are present in corresponding ratios to the layer thickness. An SEM image, Figure 4c, was taken of the ABC nanolaminate device to validate that the patterned device closely matches the optimal plasmonic shape found through the deep learning algorithm. The SEM shows that there is a slight variation between the fabricated patterns and the designed pattern. This is due to an understandable difficulty in precise fabrication at the sub-100 nm range. The Supporting Information further explains why this was not a cause for concern. Figure 4d is the measured linear transmission response for the ABC device under both TM- and TEpolarized illumination at normal incidence. As the refractive index of the ABC nanolaminate (n = 1.714) and alumina (n = 1.714)1.7591) are similar, the linear responses are as well. The linear transmission response for the control device can be found in the Supporting Information. Comparing Figures 3c and 4d, we can see that the simulated and experimental linear responses are in agreement. The slight differences are due to fabrication irregularities, which are to be expected but do not indicate that the fabricated patterns are wildly different from the designed patterns. The linear responses also indicate that the maximum SHG response for the ABC device should be expected at a wavelength 840 nm due to the resonance. The resonance in the linear response indicates that the plasmonic structure leads to the most extinction of light at the peak.

The optical nonlinear characterization in Figure 4e is the SHG response from the ABC nanolaminate. The device is excited by a fundamental wavelength, λ_{ω} , ranging from 740 to 940 nm, with a step size of 10 nm, from TM-polarized laser pulses at a constant intensity. The blue dots represent the SHG response from the patterned ABC device, the red dots represent the frequency doubled output from the patterned control device, and the cyan dots represent the generated second-harmonic signal from the unpatterned ABC surface. The SHG values were evaluated by photon counting the intensity of the signal and clearly show enhancement of the unpatterned ABC surface. The last column of panels, Figure 4f, contains the power dependence plot for the ABC device. The plot shows the relationship between the fundamental light that is input, I_{ω} , and the intensity of the output SHG response, $I_{2\omega}$, on a log-log scale. The solid line represents $I_{2\omega} \propto I_{\omega}^{K}$, where K = 2, and the quadratic dependency verifies the second-order nature of the signal. Referring to the SHG spectra, the maximum peaks show that the ABC device has clearly higher response, but comparing the two values is misleading. A proper comparison of the SHG response due to the plasmon induced second-harmonic response can be conducted by comparing the output polarization results of the control device and the ABC nanolaminate device.

The SHG output polarization characterization reveals the presence of an SHG signal from the ABC nanolaminate under normal incidence. Figure 5a,b shows the output polarization of the ABC device for TE- and TM-polarized incident fundamental light, respectively. The blue dots are the

experimental data taken at every 5°, and for the TEpolarization, the red peanut or two-lobe shape represents the data collected after a linear polarizer. The TM-polarization plot shows a wider shape than normally expected for an SHG signal. The peanut or two-lobe shape is expected for an SHG response, as the frequency doubled output is linked with the polarization angle. Comparing this plot to the alumina control device for TE- and TM-polarized incident fundamental light (Figure 5c,d, respectively) elucidates the difference. It is essential to realize that for, the control device, both the TMand TE-polarized incident fundamental light lead to peanut shapes with a very tight "waist", having zero waist indicates the light is linearly polarized, along the TM- and TE-polarization, respectively. For the patterned ABC device with incident TEpolarization, it is easy to see that, while similar to the control device, the waist of the peanut is wider, or no longer perfectly linearly polarized, with a nonzero ellipticity. Analyzing the incident TM-polarized fundamental light figure gives us a better insight into the phenomena.

In Figure 5b, the red curve represents the peanut best fit curve from the control device; we can refer to that as the polarization due to the gold pattern. The green dots in the figure were calculated by subtracting the measured SHG due to the gold pattern, from the measured SHG response of the patterned ABC device, to find the SHG response stemming solely from the ABC nanolaminate. The circle best fits the calculated data. Referring to the output polarization of the incident TE-polarized fundamental light, we can see there must be a very small circle relating to the ABC composite polarization present there too. This shows that there is a large presence of the SHG response due to the gold pattern, which is why the earlier comparison of the $\Delta I_{2\omega}$ from the SHG spectra was misleading. To separate the SHG response from the plasmonic structure and the induced SHG response of the ABC composite, the output polarization with incident TMpolarized fundamental light is crucial.

CONCLUSION

In summary, we have demonstrated an inversely designed plasmonic structure that maximizes the second-harmonic generation in an ABC nanolaminate nonlinear metamaterial. Further, we were able to differentiate the optical nonlinear response due to the plasmonic structure, and the response due to the $\chi^{(2)}$ of the ABC nanolaminate. The deep learning algorithm is a robust and flexible means for inverse design tasks that can lead to exciting metamaterial designs. Traditional guess-and-check methods involving parameter sweeping and simple geometries cannot guarantee optimal results for complex nonlinear responses. Occasionally, traditional methods also cannot reach a solution for certain desired optical responses. The deep learning framework utilized in this research is a capable instrument that can be applied to a variety of nonlinear optical responses and more challenging applications. It is important to note that a single unit structure is designed and described in this research. There have been many multiunit structures identified and studied for plasmonic and nonlinear optical purposes, including meta-lens and antenna structures. $^{37-39}$ Multiunit patterns can increase the applications of the research and allow for more precise optimization and more unique structures. However, this research specifically highlighted single unit structures in order to simplify the algorithm and to show the enhancement of nonlinear generation of light in the ABC nanolaminate

through the use of an inversely designed plasmonic structure is possible and successful. Using the deep learning algorithm, our results represent the ability to optimize and demonstrate the nonlinear optical response of a thin-film nonlinear material using a plasmonic metamaterial device. The plasmonic ABC nanolaminate structure also allows for further investigation of optical phenomena that can be applied to areas such as integrated optics, as the ABC nanolaminate is compatible with inorganic materials and CMOS technology. The results of this research expand the scope of inverse design applications and shows the potential for unconventional optical nonlinear phenomena.

EXPERIMENTAL SECTION/METHODS

Device Fabrication. The fabrication process starts with depositing ABC nanolaminates on the glass substrate (Corning, C1737 glass) via atomic layer deposition technique (Cambridge Fiji Plasma Atomic Layer Deposition System). The ABC layer is composed of 3.57 Å of TiO₂, 9.56 Å of Al₂O₃, and 9.11 Å of HfO₂ layer, and the ABC layer deposition is repeated 34 times to get a 756 Å thickness of the ABC nanolaminate, following the material and geometric parameters of the ABC from Alloatti et al. More detailed information is described in the Supporting Information. After the ABC nanolaminate is fabricated, the gold nanoparticles are formed on top of the nanolaminates in a three-step process: (i) standard electron beam lithography (E-beam litho., Elionix ELS-G100 EBL system) using poly(methyl methacrylate) (PMMA) as the positive tone electron resist, (ii) E-beam evaporation of 3 nm/45 nm Cr/Au metal, and (iii) an overnight lift-off process in acetone to resolve the plasmonic structures.

Linear Optical Characterization. A tungsten halogen lamp (B&W Tek BPS 120) is used as a broadband light source to characterize the linear response of the device. The polarization of the input light source is controlled by a set of linear polarizers and half waveplates. The transmittance spectra of the device at a normal incident angle is focused on the sample using 10× objective (NA: 0.25) and collected with a 20× objective (NA: 0.4). The light collected by the objective is delivered to the spectroscopy system (Princeton Instrument Acton SP 2300i with PIXIS 400B camera). For the reflectance spectra of the device, a 20× objective (NA: 0.4) is used to both focus and collect the light.

Nonlinear Optical Characterization. The excitation source for the nonlinear optical characterization is a tunable Ti:sapphire ultrafast oscillator (Spectra-Physics, Mai Tai HP, 690-1040 nm) with a 100 fs pulse duration and 80 MHz repetition rate. The power and polarization state are controlled by a set of halfwave plates and a Glan polarizer. The fundamental beam is delivered and focused on the device via a 10× objective (NA: 0.25), which results in a spot size of \sim 20 μ m on the sample. Both the fundamental light and the harmonic generated light from the sample are collected by a 20× objective (NA: 0.4), where the fundamental wave is eliminated as it passes through the bandpass filter. The harmonic signal is then characterized by the detector system which is composed of a monochromator (Princeton Instruments, IsoPlane) with a charge-coupled device (CCD) camera (Princeton Instruments, Pixis 400B). The state of polarization of the harmonic generated signal is analyzed by using a rotating polarizer. The peanut or lobe-shaped pattern shown in the polar diagram was formed by collecting the portion of the intensity of the harmonic generated light that passes through the rotating polarizer.

Simulator. The data set created by this study is available from the corresponding author upon reasonable request.

ASSOCIATED CONTENT

Solution Supporting Information

The Supporting Information is available free of charge at https://pubs.acs.org/doi/10.1021/acsnano.1c09298.

Additional experimental details, materials, methods, and calculations; simulator optimization and convergence details (PDF)

AUTHOR INFORMATION

Corresponding Author

Wenshan Cai — School of Electrical and Computer Engineering, Georgia Institute of Technology, Atlanta, Georgia 30332, United States; School of Materials Science and Engineering, Georgia Institute of Technology, Atlanta, Georgia 30332, United States; oocid.org/0000-0002-6367-3857; Email: wcai@gatech.edu

Authors

Lakshmi Raju – School of Electrical and Computer Engineering, Georgia Institute of Technology, Atlanta, Georgia 30332, United States

Kyu-Tae Lee — School of Electrical and Computer Engineering, Georgia Institute of Technology, Atlanta, Georgia 30332, United States; orcid.org/0000-0001-7840-0846

Zhaocheng Liu — School of Electrical and Computer Engineering, Georgia Institute of Technology, Atlanta, Georgia 30332, United States; orcid.org/0000-0001-6623-9231

Dayu Zhu — School of Electrical and Computer Engineering, Georgia Institute of Technology, Atlanta, Georgia 30332, United States

Muliang Zhu — School of Electrical and Computer Engineering, Georgia Institute of Technology, Atlanta, Georgia 30332, United States

Ekaterina Poutrina – UES, Inc, Dayton, Ohio 45432, United States; Air Force Research Laboratory, Wright-Patterson Air Force Base, Dayton, Ohio 45433, United States

Augustine Urbas — Air Force Research Laboratory, Wright-Patterson Air Force Base, Dayton, Ohio 45433, United States

Complete contact information is available at: https://pubs.acs.org/10.1021/acsnano.1c09298

Author Contributions

^OL.R. and K.-T.L. contributed equally to this work

The authors declare no competing financial interest.

ACKNOWLEDGMENTS

This work was supported in part by the National Science Foundation under grant no. DMR-2004749 and by the Office of Naval Research under grant no. N00014-17-1-2555. L.R. acknowledges the support of the National Science Foundation Graduate Research Fellowship under grant no. DGE-1650044. The authors are grateful for the support of the AFRL Minority Leadership—Research Collaboration Program and TOPS V Program, ForWarD to Materials Data Science and Informatics (FWD-MDSI), administered by ARCTOS Technology Solutions (formerly Universal Technology Corporation) under Task Order FA8650-19-F-5830 (TO 0005).

REFERENCES

- (1) Chung, J.; Gulcehre, C.; Cho, K.; Bengio, Y. Empirical evaluation of gated recurrent neural networks on sequence modeling. *arXiv.org*; 2014, 1412.3555; http://arxiv.org/abs/1412.3555 (accessed February 9, 2022).
- (2) Goodfellow, I.; Bengio, Y.; Courville, A. Deep Learning; MIT Press: Cambridge, 2016.

- (3) Hansen, L. K.; Salamon, P. Neural network ensembles. *IEEE Transactions on Pattern Analysis & Machine Intelligence* **1990**, 12, 993–1001.
- (4) Herz, A. V.; Gollisch, T.; Machens, C. K.; Jaeger, D. Modeling single-neuron dynamics and computations: a balance of detail and abstraction. *Science* **2006**, *314*, 80–85.
- (5) LeCun, Y.; Bengio, Y.; Hinton, G. Deep learning. *Nature* **2015**, 521, 436–444.
- (6) Voulodimos, A.; Doulamis, N.; Doulamis, A.; Protopapadakis, E. Deep Learning for Computer Vision: A Brief Review. *Computational Intelligence and Neuroscience* **2018**, 2018, 7068349.
- (7) Young, T.; Hazarika, D.; Poria, S.; Cambria, E. Recent Trends in Deep Learning Based Natural Language Processing. *IEEE Computational Intelligence Magazine* **2018**, *13*, 55–75.
- (8) Carrasquilla, J.; Melko, R. G. Machine learning phases of matter. *Nat. Phys.* **2017**, *13*, 431–434.
- (9) Chen, Y.; Lin, Z.; Zhao, X.; Wang, G.; Gu, Y. Deep Learning-Based Classification of Hyperspectral Data. *IEEE Journal of Selected Topics in Applied Earth Observations and Remote Sensing* **2014**, 7, 2094–2107.
- (10) Krizhevsky, A.; Sutskever, I.; Hinton, G. E. ImageNet classification with deep convolutional neural networks. *Commun. ACM* **2017**, *60*, 84–90.
- (11) Liu, D.; Tan, Y.; Khoram, E.; Yu, Z. Training Deep Neural Networks for the Inverse Design of Nanophotonic Structures. ACS Photonics 2018, 5, 1365–1369.
- (12) Sanchez-Lengeling, B.; Aspuru-Guzik, A. Inverse molecular design using machine learning: Generative models for matter engineering. *Science* **2018**, *361*, *360*–*365*.
- (13) Forestiere, C.; Pasquale, A. J.; Capretti, A.; Miano, G.; Tamburrino, A.; Lee, S. Y.; Reinhard, B. M.; Dal Negro, L. Genetically Engineered Plasmonic Nanoarrays. *Nano Lett.* **2012**, *12*, 2037–2044.
- (14) Malkiel, I.; Mrejen, M.; Nagler, A.; Arieli, U.; Wolf, L.; Suchowski, H. Plasmonic nanostructure design and characterization via Deep Learning. *Light: Science & Applications* **2018**, *7*, 60.
- (15) Zhao, H.; Liu, H.; Hu, W.; Yan, X. Anomaly detection and fault analysis of wind turbine components based on deep learning network. *Renewable Energy* **2018**, *127*, 825–834.
- (16) Gong, Z.; Li, C.; Hu, X.; Yang, H.; Gong, Q. Active control of highly efficient third-harmonic generation in ultrathin nonlinear metasurfaces. *Opt. Mater.* **2016**, *60*, 552–558.
- (17) Hooper, D. C.; Kuppe, C.; Wang, D.; Wang, W.; Guan, J.; Odom, T. W.; Valev, V. K. Second Harmonic Spectroscopy of Surface Lattice Resonances. *Nano Lett.* **2019**, *19*, 165–172.
- (18) Timbrell, D.; You, J. W.; Kivshar, Y. S.; Panoiu, N. C. A comparative analysis of surface and bulk contributions to second-harmonic generation in centrosymmetric nanoparticles. *Sci. Rep.* **2018**, *8*, 3586.
- (19) Rui, G.; Abeysinghe, D. C.; Nelson, R. L.; Zhan, Q. Demonstration of beam steering via dipole-coupled plasmonic spiral antenna. *Sci. Rep.* **2013**, *3*, 2237.
- (20) Zhu, X.; Zhang, J.; Xu, J.; Li, H.; Wu, X.; Liao, Z.; Zhao, Q.; Yu, D. Dispersion Control in Plasmonic Open Nanocavities. *ACS Nano* **2011**, *5*, 6546–6552.
- (21) Munechika, K.; Chen, Y.; Tillack, A. F.; Kulkarni, A. P.; Plante, I. J.-L.; Munro, A. M.; Ginger, D. S. Spectral Control of Plasmonic Emission Enhancement from Quantum Dots near Single Silver Nanoprisms. *Nano Lett.* **2010**, *10*, 2598–2603.
- (22) Alloatti, L.; Kieninger, C.; Froelich, A.; Lauermann, M.; Frenzel, T.; Köhnle, K.; Freude, W.; Leuthold, J.; Wegener, M.; Koos, C. Second-order nonlinear optical metamaterials: ABC-type nanolaminates. *Appl. Phys. Lett.* **2015**, *107*, 121903.
- (23) Clemmen, S.; Hermans, A.; Solano, E.; Dendooven, J.; Koskinen, K.; Kauranen, M.; Brainis, E.; Detavernier, C.; Baets, R. Atomic layer deposited second-order nonlinear optical metamaterial for back-end integration with CMOS-compatible nanophotonic circuitry. *Opt. Lett.* **2015**, *40*, 5371–5374.
- (24) Hermans, A.; Kieninger, C.; Koskinen, K.; Wickberg, A.; Solano, E.; Dendooven, J.; Kauranen, M.; Clemmen, S.; Wegener, M.;

- Koos, C.; Baets, R. On the determination of $\chi^{(2)}$ in thin films: a comparison of one-beam second-harmonic generation measurement methodologies. *Sci. Rep.* **2017**, *7*, 44581.
- (25) Hsiao, H.-H.; Abass, A.; Fischer, J.; Alaee, R.; Wickberg, A.; Wegener, M.; Rockstuhl, C. Enhancement of second-harmonic generation in nonlinear nanolaminate metamaterials by nanophotonic resonances. *Opt. Express* **2016**, *24*, 9651–9659.
- (26) Chen, Y.; Hu, Y.; Zhao, J.; Deng, Y.; Wang, Z.; Cheng, X.; Lei, D.; Deng, Y.; Duan, H. Topology Optimization-Based Inverse Design of Plasmonic Nanodimer with Maximum Near-Field Enhancement. *Adv. Funct. Mater.* **2020**, *30*, 2000642.
- (27) Sitawarin, C.; Jin, W.; Lin, Z.; Rodriguez, A. W. Inverse-designed photonic fibers and metasurfaces for nonlinear frequency conversion. *Photon. Research* **2018**, *6*, B82–B89.
- (28) Wang, R.; Liang, F.; Lin, Z. Data-driven prediction of diamond-like infrared nonlinear optical crystals with targeting performances. *Sci. Rep.* **2020**, *10*, 3486.
- (29) Xu, L.; Rahmani, M.; Ma, Y.; Smirnova, D. A.; Kamali, K. Z.; Deng, F.; Chiang, Y. K.; Huang, L.; Zhang, H.; Gould, S.; Neshev, D. N.; Miroshnichenko, A. E. Enhanced light—matter interactions in dielectric nanostructures via machine-learning approach. *Advanced Photonics* **2020**, *2*, 026003.
- (30) Carletti, L.; Zilli, A.; Moia, F.; Toma, A.; Finazzi, M.; De Angelis, C.; Neshev, D. N.; Celebrano, M. Steering and Encoding the Polarization of the Second Harmonic in the Visible with a Monolithic LiNbO3Metasurface. *ACS Photonics* **2021**, *8*, 731–737.
- (31) Zhang, Y.; Grady, N. K.; Ayala-Orozco, C.; Halas, N. J. Three-Dimensional Nanostructures as Highly Efficient Generators of Second Harmonic Light. *Nano Lett.* **2011**, *11*, 5519–5523.
- (32) Liu, Z.; Raju, L.; Zhu, D.; Cai, W. A Hybrid Strategy for the Discovery and Design of Photonic Structures. *IEEE Journal on Emerging and Selected Topics in Circuits and Systems* **2020**, *10*, 126–135.
- (33) Piggott, A. Y.; Lu, J.; Lagoudakis, K. G.; Petykiewicz, J.; Babinec, T. M.; Vučković, J. Inverse design and demonstration of a compact and broadband on-chip wavelength demultiplexer. *Nat. Photonics* **2015**, *9*, 374–377.
- (34) Boyd, R. W. Nonlinear Opt., 3rd ed.; Academic Press: Amsterdam; Boston, 2008.
- (35) Kingma, D. P.; Welling, M. Auto-Encoding Variational Bayes. arXiv; 2014; 1312.6114; https://arxiv.org/abs/1312.6114 (accessed February 9, 2022).
- (36) Wiecha, P. R.; Arbouet, A.; Girard, C.; Lecestre, A.; Larrieu, G.; Paillard, V. Evolutionary multi-objective optimization of colour pixels based on dielectric nanoantennas. *Nat. Nanotechnol.* **2017**, *12*, 163–169.
- (37) Chen, X.; Huang, L.; Mühlenbernd, H.; Li, G.; Bai, B.; Tan, Q.; Jin, G.; Qiu, C.-W.; Zhang, S.; Zentgraf, T. Dual-polarity plasmonic metalens for visible light. *Nat. Commun.* **2012**, *3*, 1198.
- (38) Zhu, D.; Liu, Z.; Raju, L.; Kim, A. S.; Cai, W. Building Multifunctional Metasystems via Algorithmic Construction. *ACS Nano* **2021**, *15*, 2318–2326.
- (39) Nazirzadeh, M. A.; Atar, F. B.; Turgut, B. B.; Okyay, A. K. Random sized plasmonic nanoantennas on Silicon for low-cost broadband near-infrared photodetection. *Sci. Rep.* **2015**, *4*, 7103.